JOURNAL OF AIRCRAFT
Vol. 31, No. 3, May–June 1994

Computation of Three-Dimensional Hypersonic Flows in Chemical Nonequilibrium

S. Menne,* C. Weiland,† and M. Pfitzner‡
Deutsche Aerospace A.G., Space Division, W-8000 Munich 80, Germany

An algorithm for the simulation of three-dimensional hypersonic flows in chemical nonequilibrium is presented. The basic flow solver is based on a quasiconservative formulation of the Euler or Navier-Stokes equations. The Jacobi matrices are split according to the sign of their eigenvalues. The derivatives of the conservative variables are split accordingly. A third-order upwind space discretization is used in conjunction with an optimized three-stage Runge-Kutta explicit time stepping scheme. The chemistry source terms are treated point-implicitly. For inviscid flow, the code is applied to the complete HERMES 1.0 configuration. The influence of mesh resolution is studied by comparing a fine grid with a coarse grid solution. The coarse grid solution is usually sufficient to describe global flow phenomena. The analysis of local flow details requires refined meshes. For viscous flow, the flow about generic configurations (double-ellipse, hemisphere-cylinder-flare, hyperbola-flare) is investigated by performing grid sensitivity studies as well as by comparing different transport models.

I. Introduction

DUE to the initiation of the HERMES program, large research efforts have been directed to the development of space vehicles in Europe. The re-entry trajectories for space vehicles include large regions where the airflow is in chemical and thermal nonequilibrium. Nonequilibrium effects are important when the time scale for chemical reactions or energy exchange t_{chem} is comparable to a characteristic time scale for global flow changes t_{flow}. If $t_{chem} << t_{flow}$, the process is in equilibrium, and if $t_{chem} >> t_{flow}$, the process is frozen. Since the density of air is low and the vehicle velocity on the re-entry trajectory is high in the upper atmosphere, nonequilibrium effects have to be considered for altitudes larger than about 50 km. It is important to take nonequilibrium influences into account in order to be able to correctly simulate the aerodynamic behavior (pitching moment, c.p.), as well as heat-loads on the surface of the space vehicle (recombination, wall catalycity, radiation) at high altitudes. Although thermal nonequilibrium may be important near the vehicle nose and may influence the subsequent flowfield by convection, it is neglected here. Especially for the heat loads, a viscous flow simulation is necessary because the flow in the immediate vicinity of the vehicle surface is viscosity dominated.

The numerical simulation of nonequilibrium real gas flows requires very specialized and detailed physical models and numerical methods. Due to the complicated numerical formulation, code implementation, and due to the excessive computational requirements for numerical calculations, only recently nonequilibrium reacting flow computations have been undertaken. Numerical methods implemented so far use a full-conservative flux-splitting approach for the convective fluxes (either flux-vector or flux-difference).[1–6] The intention of the work described in this article was to develop a solution method and computer code for the numerical simulation of nonequilibrium real gas flows about the complete HERMES configuration based on earlier developments for perfect gas flows[7,8] and equilibrium real gas flows.[9,10] In contrast to other solution methods, we employ the quasiconservative formulation with matrix splitting originally developed by Weiland[7] and the shock-fitting technique implemented by Pfitzner,[11] which is a post-correction technique based on the ideas of Pandolfi.[12] The quasiconservative matrix splitting technique allows an accurate flow description in both inviscid and viscosity dominated regions. Using the shock-fitting technique, the location of the bow shock is given precisely. This is especially important for local bow shock—structure interactions (e.g., bow shock—winglet interaction). Additionally, the shock-fitting procedure enhances the efficiency of the method by limiting the computational domain automatically to the region where flow changes occur. In the near future, the solution method will be extended to include thermal nonequilibrium as well as advanced wall catalycity models and models for the transport terms. This work will be performed in the frame of the HERMES technology program in cooperation with international partners.

In Sec. II we describe the physical model for viscous flows in chemical nonequilibrium (equation of state, chemistry terms, transport terms). In Sec. III we present the solution method (mixed quasi-/full-conservative formulation, matrix splitting, and discretization). Results are shown in Sec. IV for inviscid flows about the complete HERMES configuration and for viscous flows over generic configurations. A general conclusion is given in Sec. V.

II. Governing Equations

The governing equations for viscous flow in chemical nonequilibrium read

$$\frac{\partial}{\partial t} Q + \sum_{i=1}^{3} \frac{\partial}{\partial x_i} (F_{I,xi} - F_{v,xi}) = S \tag{1}$$

with the conservative variables Q

$$Q = (\rho, \rho v_{x1}, \rho v_{x2}, \rho v_{x3}, \rho_1, \ldots, \rho_{ns}, e)^T \tag{2}$$

the source term S

$$S = (0, 0, 0, 0, \dot{\omega}_1, \ldots, \dot{\omega}_{ns}, 0)^T \tag{3}$$

Received May 22, 1992; presented as Paper 92-2876 at the AIAA 27th Thermophysics Conference, Nashville, TN, July 6–8, 1992; revision received May 27, 1993; accepted for publication May 27, 1993.

*Research Scientist, Department RTT314, P.O. Box 80 11 69. Member AIAA.

†Head of Propulsion Systems, Department RTT31, P.O. Box 80 11 69.

‡Research Scientist; currently at BMW—Rolls-Royce GmbH, W-8044 Lohhof, Germany.

the inviscid fluxes

$$F_{I,xi} = [\rho v_{xi}, m_{xi,1}, m_{xi,2}, m_{xi,3}, \rho_1 v_{xi}, \ldots, \rho_{ns} v_{xi}, (e + p)v_{xi}]^T \tag{4}$$

$$m_{xi,j} = \rho v_{xi} v_{xj} + \delta_{i,j} p, \qquad i, j = 1, \ldots, 3 \tag{5}$$

and the viscous fluxes

$$F_{v,xi} = (0, \tau_{xi,x1}, \tau_{xi,x2}, \tau_{xi,x3}, j_{1,xi}, \ldots, j_{ns,xi}, \sum v_{xj}\tau_{xi,xj} - q_{xi} + d_{xi})^T \tag{6}$$

with the Kronecker operator $\delta_{i,j}$. The usual notation is adopted here, i.e., ρ denotes the total density, ρ_s are the species densities with $s = 1, \ldots, n_s$, and n_s being the number of species in the mixture. v_{x1}, v_{x2}, v_{x3} are the Cartesian velocity components in the x_1, x_2, x_3 directions, respectively, p is the static pressure, e is the total energy, $\dot{\omega}_s$ is the source term for species s, $\bar{\bar{\tau}}$ is the stress tensor, q is the heat flux, j_s is the diffusion term of species s, and d is the enthalpy diffusion.

A. Equation of State

The total enthalpy H is defined by

$$H = [(e + p)/\rho] \tag{7}$$

The internal enthalpy of the mixture is coupled with the species internal enthalpies via

$$h = H - \frac{1}{2} v^2 = \sum_{s=1}^{ns} y_s h_s(T) \tag{8}$$

where the mass concentrations $y_s = \rho_s/\rho$, and the species internal enthalpies depend on the mixture temperature only. The species enthalpies contain contributions from equilibrium vibrational degrees of freedom (DOF) and the heat of formation. We employ both the fit coefficients given in the HERMES Antibes workshop and those developed by Warnatz.[13]

We assume that each species can be considered as an ideal gas, i.e., the equation of state reads

$$p = \rho \bar{R} T \sum_{s=1}^{ns} \frac{y_s}{M_s} = \rho \bar{R} T \mathfrak{L} \tag{9}$$

where $\bar{R}$ is the universal gas constant $\bar{R} = 8.31441$ J/g-mole-K, and M_s is the molar mass of the sth species. The mixture density ρ is the sum of all species densities. Equations (7–8) can be combined yielding

$$\rho h = e + p - \frac{\rho}{2} v^2 = \sum_{s=1}^{ns} \rho_s h_s(T) \tag{10}$$

Inserting the equation of state (9) into (10) leads to a nonlinear equation for either p or T which can be solved by a simple Newton iteration.[14]

B. Chemistry Terms

The reacting air is modeled using the five species (N_2, N, O_2, O, NO) and the 17 nonionizing reactions model from Park.[15,16] Currently, the code uses the assumption of thermal equilibrium of the vibrational DOF. For chemical reactions of n_s species in n_r reactions

$$\sum_{s=1}^{ns} \left(\alpha_{s,r} \frac{\rho_s}{M_s}\right) \leftrightarrow \sum_{s=1}^{ns} \left(\beta_{s,r} \frac{\rho_s}{M_s}\right), \qquad r = 1, \ldots, n_r \tag{11}$$

the source terms are of the form[17]

$$\dot{\omega}_s = M_s \sum_{r=1}^{nr} [(\beta_{s,r} - \alpha_{s,r}) J_r], \qquad s = 1, \ldots, n_s \tag{12}$$

with

$$J_r = \Omega_{f,r} - \Omega_{b,r}, \qquad r = 1, \ldots, n_r \tag{13}$$

$$\Omega_{f,r} = k_{f,r}(T) \prod_{s=1}^{ns} \left(\frac{\rho_s}{M_s}\right)^{\alpha_{s,r}} \tag{14}$$

$$\Omega_{b,r} = k_{b,r}(T) \prod_{s=1}^{ns} \left(\frac{\rho_s}{M_s}\right)^{\beta_{s,r}} \tag{15}$$

The backward reaction rate coefficient $k_b(T)$ is calculated from the temperature fits to the forward reaction rate coefficient $k_f(T)$ and the equilibrium constants $K_c(T)$[15]

$$k_{b,r}(T) = k_{f,r}(T)/K_{c,r}(T) \tag{16}$$

The point-implicit treatment of the chemical source terms includes the dependence of the source terms on the species densities only. The $\dot{\omega}_s$ depend on the ρ_s explicitly via the product terms in Eqs. (14) and (15), and implicitly via the temperature dependence of the chemical rates $k(T)$. Normally, the temperature dependence can be neglected, but in an equilibrium flow situation it has to be taken into account. The derivative of the source terms with respect to the species mass densities is evaluated as follows. Applying the chain rule to expression (14) and replacing the product in Eq. (14) by $\Omega_{f,r}/k_{f,r}$, we have

$$\frac{\partial \dot{\omega}_i}{\partial \rho_j} = M_i \sum_{r=1}^{nr} \left[(\beta_{i,r} - \alpha_{i,r}) \frac{\partial J_r}{\partial \rho_j}\right] \tag{17}$$

$$\frac{\partial J_r}{\partial \rho_j} = \frac{1}{\rho_j} (\alpha_{j,r}\Omega_{f,r} - \beta_{j,r}\Omega_{b,r}) + \frac{\partial T}{\partial \rho_j} \left[\frac{\partial \log(k_f)}{\partial T} \Omega_{f,r} - \frac{\partial \log(k_b)}{\partial T} \Omega_{b,r}\right] \tag{18}$$

The second term in Eq. (18) is dropped if the dependence of the temperature on the species densities can be neglected.

C. Transport Terms and Transport Coefficients

The diffusion term in the species equation is

$$j_{s,xi} = \rho D_s \frac{\partial X_s}{\partial x_i} \tag{19}$$

where D_s is the species diffusion coefficient and X_s is the mole fraction. The enthalpy diffusion d appears in the total energy equation

$$d_{xi} = \rho \sum_{s=1}^{ns} h_s D_s \frac{\partial X_s}{\partial x_i} \tag{20}$$

and describes the diffusion of enthalpy due to concentration gradients. Fourier's law holds for the heat flux q which accounts for the conduction of energy due to temperature gradients. The stress tensor $\bar{\bar{\tau}}$ has the entries[18]

$$\tau_{xi,xj} = \mu \left(\frac{\partial v_{xj}}{\partial x_j} + \frac{\partial v_{xj}}{\partial x_i}\right) - \frac{2}{3} \delta_{i,j} \sum_k \frac{\partial v_{xk}}{\partial x_k} \tag{21}$$

where μ is the mixture viscosity. The bulk viscosity is assumed to be zero (Stokes hypothesis), although this assumption is questionable for a nonequilibrium real gas.[17]

The species viscosities are represented employing Blottner's fits.[19] The curve fits are appropriate for temperatures up to 10,000 K and for weak ionization. The heat conduction coefficient η is found using Eucken's correction.[20] Wilke's for-

mula [21] is employed for the mixture viscosity and the mixture heat conduction. For the diffusion coefficient, we assume that the diffusion coefficients for the species are identical[22] and that the Schmidt number is equal to one.[23] Alternately, we use the model of Yos[24] which is based on the evaluation of collision integrals for all kinds of particle interaction. The collision integrals are evaluated as curve fits as proposed in Gnoffo et al.[25] This model provides all necessary transport coefficients.

Work is in progress to improve the transport models and the relation for the transport coefficients. One progress direction is generality, i.e., to account for thermal nonequilibrium influences in the transport terms, the other direction is consistency, i.e., to formulate the transport models in a way consistent with the governing equations. It is not trivial, e.g., to fulfill the condition that the sum of the species diffusions has to vanish in the mixture continuity equation.

III. Solution Method

To solve the governing equations for realistic flow cases, we introduce curvilinear coordinates ξ_1, ξ_2, ξ_3

$$\xi_i = \xi_i(x_1, x_2, x_3; \quad t) \tag{22}$$

$$\tau = t \tag{23}$$

Employing the metric Jacobian

$$J = \frac{\partial(\xi_1, \xi_2, \xi_3)}{\partial(x_1, x_2, x_3)} \tag{24}$$

the metric derivatives read

$$\frac{1}{J}\frac{\partial \xi_j}{\partial x_i} = \frac{\partial x_{\bar{i}+1}}{\partial \xi_{\bar{j}+1}}\frac{\partial x_{\bar{i}+2}}{\partial \xi_{\bar{j}+2}} - \frac{\partial x_{\bar{i}+1}}{\partial \xi_{\bar{j}+2}}\frac{\partial x_{\bar{i}+2}}{\partial \xi_{\bar{j}+1}}$$
$$\bar{i} = 1 + \text{mod}(i - 1, 3) \tag{25}$$

$$\frac{\partial \xi_i}{\partial t} = -\sum_{j=1}^{3} \frac{\partial \xi_i}{\partial x_j}\frac{\partial x_j}{\partial \tau} \tag{26}$$

Introducing the metric relations into the governing equations, we get, after some arrangements, the full conservative form in curvilinear coordinates

$$\frac{\partial}{\partial \tau}\left(\frac{1}{J}Q\right) + \sum_{i=1}^{3}\frac{\partial F_{I,\xi_i}}{\partial \xi_i} = \frac{1}{J}S + \sum_{i=1}^{3}\frac{\partial F_{v,\xi_i}}{\partial \xi_i} \tag{27}$$

with the generalized fluxes ($k = \xi_1, \xi_2, \xi_3$)

$$F_{I,k} = \frac{k_t}{J}Q + \sum_{i=1}^{3}\frac{k_{x_i}}{J}F_{I,x_i} \tag{28}$$

$$F_{v,k} = \sum_{i=1}^{3}\frac{k_{x_i}}{J}F_{v,x_i} \tag{29}$$

Note that we adopt here the convention that metric derivatives may be written in subscript notation, i.e., $k_{x_i} \equiv (\partial k/\partial x_i)$. This notation is used exclusively for the metric terms.

The inviscid fluxes read

$$F_{I,k} = (k_t/J)Q + (1/J)\begin{bmatrix} \rho\Theta_k \\ \rho v_{x_1}\Theta_k + k_{x_1}p \\ \rho v_{x_2}\Theta_k + k_{x_2}p \\ \rho v_{x_3}\Theta_k + k_{x_3}p \\ \rho_1\Theta_k \\ \vdots \\ \rho_{n_s}\Theta_k \\ \Theta_k(e + p) \end{bmatrix} \tag{30}$$

with the contravariant velocity component

$$\Theta_k = \sum_{i=1}^{3} k_{x_i} v_{x_i} \tag{31}$$

The viscous fluxes $F_{v,k}$

$$F_{v,k} = (f_1, f_2, f_3, f_4, f_{4+1}, \ldots, f_{4+n_s}, f_{5+n_s})^T \tag{32}$$

can be expressed as

$$f_1 = 0 \tag{33}$$

$$f_l = \frac{\mu}{J}\sum_{i=1}^{3}\sum_{j=1}^{3}\alpha_{ij}^{l}\frac{\partial v_{x_i}}{\partial \xi_j}, \qquad l = 2, \ldots, 4 \tag{34}$$

$$f_{4+s} = \frac{\rho}{J}D_s\sum_{i=1}^{3}\frac{\partial X_s}{\partial \xi_i}a_{\xi_i}, \qquad s = 1, \ldots, n_s \tag{35}$$

$$f_{5+n_s} = \sum_{i=1}^{3} v_{x_i} f_{i+1} + \sum_{s=1}^{n_s} h_s f_{4+s} + \frac{\eta}{J}\sum_{i=1}^{3}\frac{\partial T}{\partial \xi_i}a_{\xi_i} \tag{36}$$

where the metric terms a_{ξ_i}, and α_{ij}^{l} are introduced for abbreviation

$$a_{\xi_j} = \sum_{i=1}^{3}\frac{\partial k}{\partial x_i}\frac{\partial \xi_j}{\partial x_i} \tag{37}$$

$$\alpha_{ij}^{l} = \delta_{l,i}(a_{\xi_j} + b_{\xi_j,x_i} - c_{\xi_j,x_i,x_l}) + c_{\xi_j,x_i,x_l} \tag{38}$$

$$b_{\xi_j,x_i} = \frac{1}{3}\frac{\partial k}{\partial x_i}\frac{\partial \xi_j}{\partial x_i} \tag{39}$$

$$c_{\xi_j,x_i,x_l} = \frac{\partial k}{\partial x_i}\frac{\partial \xi_j}{\partial x_l} - \frac{2}{3}\frac{\partial k}{\partial x_l}\frac{\partial \xi_j}{\partial x_i} \tag{40}$$

Since for Euler flows the quasiconservative formulation[7,8] has been proven to be very accurate,[9,10,26] we use the same form for the Navier-Stokes formulation. However, the viscous fluxes in a nonconservative formulation are more complicated consisting of much more terms compared with a full conservative formulation. Therefore, we consider the viscous terms in full conservative form. The treatment of the viscous terms follows closely the formulation given in Menne[27] and Menne and Weiland.[28] The result is that we have to transform only the convective part of the governing equations into the quasiconservative form, whereas the viscous part remains fully conservative.

A. Mixed Quasi-/Full-Conservative Formulation

For abbreviation, we summarize the viscous fluxes in the governing Eq. (27) in the single term $\mathcal{R}$:

$$\mathcal{R} = \sum_{i=1}^{3}\frac{\partial}{\partial \xi_i}F_{v,\xi_i} \tag{41}$$

Applying the chain rule on the left side of Eq. (27) and using metric identities we get the final form of the governing equations which is quasiconservative for the convective part and fully conservative for the viscous part

$$\frac{\partial Q}{\partial \tau} + \sum_{i=1}^{3}A_{\xi_i}\frac{\partial Q}{\partial \xi_i} = (S + J\mathcal{R}) \tag{42}$$

The flux Jacobians A_k, $k = \xi_1, \xi_2, \xi_3$ are

$$A_k = k_t\delta_{i,j} + \sum_{i=1}^{3}k_{x_i}\frac{\partial F_{I,x_i}}{\partial Q} \tag{43}$$

In the following section we derive the matrix splitting form of the governing equations.

B. Matrix Splitting

We derive a split matrix form of the governing equations in a mixed quasi-/full-conservative form. To determine the splitting form of the governing equations, we have to determine the eigenvalues and the corresponding eigenvectors of the flux matrices. The eigenvalues of A_k are

$$\Lambda_k = \lambda_3\delta_{i,j} + (\lambda_1 - \lambda_3)\delta_{i,1}\delta_{1,j} + (\lambda_2 - \lambda_3)\delta_{i,2}\delta_{2,j} \quad (44)$$

$$\lambda_m = k_t + \Theta_k + \sigma_m c g_k \quad (45)$$

where $\sigma_m = +1, -1, 0$ for $m = 1, 2, 3$, and g_k is the norm of the metric gradient $g_k = |\nabla k|$. The eigenvalues are split into their positive and negative parts by

$$\Lambda_k^{\pm} = \frac{1}{2}(\Lambda_k \pm |\Lambda_k|) \quad (46)$$

Since the eigenvalues λ_n, $n > 2$ are strongly degenerated, it is advantageous to employ the form given in Eq. (44). The frozen speed of sound is introduced here with

$$c^2 = \frac{\left.\frac{\partial h}{\partial \rho}\right|_{p,ys}}{\frac{1}{\rho} - \left.\frac{\partial h}{\partial p}\right|_{\rho,ys}} \quad (47)$$

To compute the flux Jacobians, derivatives of the internal enthalpy w.r.t. the flow variables have to be computed. Due to the assumption of a nonequilibrium real gas whose components can be considered as ideal gases, all enthalpy derivatives can be expressed in terms of temperature derivatives of the species enthalpies. This way, only the derivative of the species enthalpy w.r.t. the temperature has to be computed. Using the eigenvalue matrices $\Lambda_k^{\pm}$, the split form can be expressed as

$$\frac{\partial Q}{\partial \tau} + \sum_{i=1}^{3} T_{\xi_i}\left(\Lambda_{\xi_i}^{+} T_{\xi_i}^{-1}\frac{\partial Q^{+}}{\partial \xi_i} + \Lambda_{\xi_i}^{-} T_{\xi_i}^{-1}\frac{\partial Q^{-}}{\partial \xi_i}\right) = (S + J\mathcal{R}) \quad (48)$$

Due to the degenerated eigenvalue λ_3, the right and left eigenvectors are arbitrary to some extent. Here, we chose the arbitrary parameters such that the eigenvector matrices reduce to the perfect gas matrices given in Whitfield and Janus[30] in the limit of a perfect gas state. A more detailed description, including the right and left eigenvector matrices, can be found in Menne et al.[29]

C. Discretization

The spatial discretization is done by third-order upwind biased differences for the convective part

$$\left.\frac{\partial Q^{\pm}}{\partial \xi_i}\right|_j = \pm\frac{1}{6\Delta\xi_i}\sum_{m=-2}^{1} a_m Q_{j\pm m} + O(\Delta\xi_i^3) \quad (49)$$

with $a_{-2} = 1$, $a_{-1} = -6$, $a_0 = 3$, and $a_1 = 2$, and by central differencing for the full conservative viscous part

$$\left.\frac{\partial F_{v,\xi_i}}{\partial \xi_i}\right|_j = \frac{1}{2\Delta\xi_i}[F_{v,j+(1/2)} - F_{v,j-(1/2)}] + O(\Delta\xi_i^2) \quad (50)$$

The time integration is performed at the present state by a Runge-Kutta time-stepping scheme. The scheme is applied to the governing equations in the form

$$\frac{\partial Q^n}{\partial \tau} = \mathcal{L}(Q^n) \quad (51)$$

where the convective part together with viscous part and source term is collected in the operator $\mathcal{L}(Q)$. The three-stage Runge-Kutta scheme used in the calculations is

$$Q^{(l)} = Q^{(0)} + \Delta\tau\alpha_l\mathcal{L}[Q^{(l-1)}] \quad (52)$$

where $l = 1, 2, 3$ denote the intermediate Runge-Kutta time step level, and the coefficients α_l are chosen to guarantee maximum stability and second-order accuracy in time, namely $\alpha_1 = 0.25$, $\alpha_2 = 0.5$, and $\alpha_3 = 1$.

IV. Results

We present inviscid flow results for the complete HERMES configuration and viscous results for generic configurations. Comparisons of experimental measurements with inviscid results obtained with a previous Euler version of the current code, e.g., nonequilibrium sphere flow and cylinder flow, can be found in Pfitzner.[11,14] Concerning computational resources requirements, the coarse grid code requires a total of 77.9 Mbyte (MB) of main memory (21.8 MB for the front part and 55.4 MB for the rear part), and the fine grid code needs 246 MB (63.3 MB front and 182.7 MB rear). The computation time depends strongly on the flow case, e.g., the (optional) point-implicit chemistry is very time consuming. Also, we use a mixed blockwise time-marching/complete iteration strategy in mostly supersonic regions. The computational effort per iteration step per grid point is about 3 ms on a IBM RS/6000-350 RISC workstation. The convergence criterion is a drop

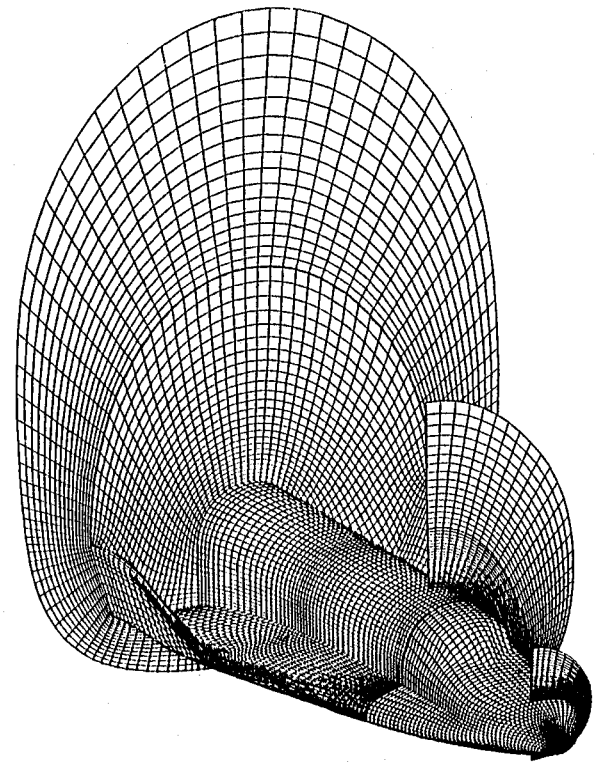

Fig. 1 HERMES 1.0, nonequilibrium Euler simulation. Surface grid (fine). $M_\infty = 20$, $\alpha = 30$ deg, $p_\infty = 2.106$ Pa, $\rho_\infty = 3.738 \times 10^{-5}$ kg/m^3.

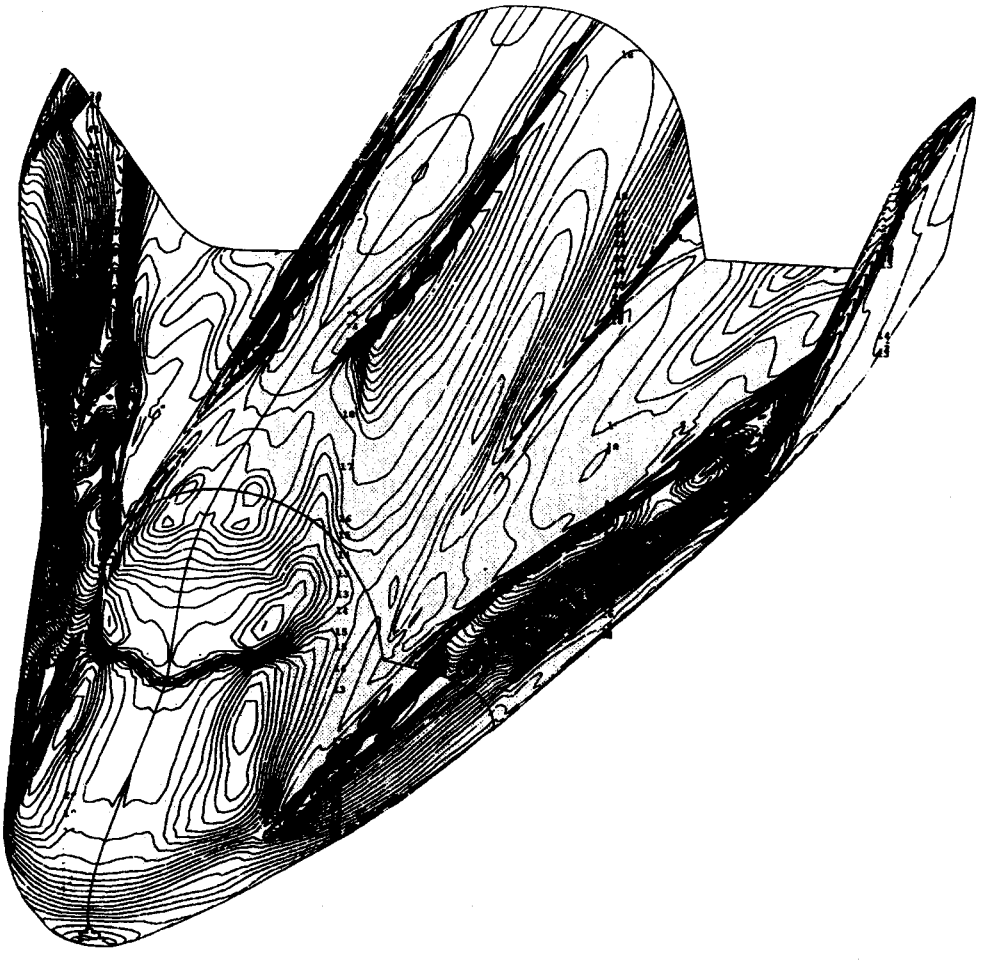

Fig. 2 HERMES 1.0, nonequilibrium Euler simulation. Surface Mach number contours (fine). $M_\infty = 20$, $\alpha = 30$ deg, $p_\infty = 2.106$ Pa, $\rho_\infty = 3.738 \times 10^{-5}$ kg/m^3.

in the residual of the continuity equation by at least four orders of magnitude.

A. HERMES 1.0 Calculations

First, we show results for inviscid flow about the complete HERMES 1.0 (shape 1.0) configuration. The freestream conditions are $p_\infty = 2.106$ Pa, $\rho_\infty = 3.738 \times 10^{-5}$ kg/m^3, $T_\infty = 196$ K, and $M_\infty = 20$ with an angle of attack $\alpha = 30$ deg. The flow simulation was done in two parts. A single block grid was employed in the front part of the vehicle. In the aft part a double block grid was used. Figure 1 displays the mesh structure with the surface grid and the mesh in three crossflow sections. Computations with two different meshes have been performed: 1) a fine grid solution with a mesh consisting of 700,222 grid points and 2) a coarse grid solution consisting of 219,626 grid points. Compared to Fig. 1, the actual coarse mesh has twice the number of grid points in streamwise direction and, additionally, the fine mesh has twice the number of grid points in circumferential direction. The quality of the solution depends strongly on the quality of the mesh, especially for the quasiconservative formulation. The HERMES mesh used for the present computations was generated by Hartmann.[31]

Figure 2 presents Mach number contours on the upper surface of HERMES (fine grid). The general flow phenomena are already captured by the coarse grid solution. However, flow details are not sufficiently resolved, e.g., the small crossflow shock near the fuselage-wing corner in the rear part of the fuselage. Figure 3 shows Mach number contours in the crossflow section $Z = 14$ m (fine grid). Critical areas for the coarse grid solution are the fuselage-wing corner and the top of the fuselage. Due to the strong expansion around the leading edge of the winglet, there is a strong recompression shock on the wing with a subsequent slip-layer which can be identified by comparing Fig. 3 and Fig. 4, where isobars [$\log(p/p_\infty)$] are displayed at the same crossflow section (fine grid). The crossflow shock on top of the fuselage is caused by the symmetry condition in the symmetry plane. The fuselage itself causes the crossflow to change its direction by forming a fuselage shock. The main differences between fine grid and coarse grid solution occur in the rear part on the leeward side as can be seen in Fig. 5 where the mixture temperature T is plotted vs the streamwise coordinate. The solid line is the coarse grid result and the squares denote the fine grid solution. The reason for the differences in the rear part is an insufficient resolution of the symmetry shock region on top of the fuselage for the coarse grid.

Figure 6 presents species concentration contours of atomic oxygen in the symmetry plane. Atomic oxygen is mostly generated on the windward side and in the nose region. On the leeward side, it is convected from the nose region (plus an additional amount generated by the canopy shock) along the streamlines away from the body surface in the rear part. Simultaneously, the strong crossflow caused by the flow expansion around the winglet pushes the flow towards the symmetry plane. The behavior of atomic nitrogen is qualitatively the same as for atomic oxygen.

The evaluation of the global coefficients for several flow cases are shown in Table 1. The cases denoted by F4 correspond to simulated F4-wind-tunnel conditions (high-enthalpy wind tunnel F4 of ONERA in Fauga/Mauzac, France). Experimental results for comparison with the wind-tunnel simulations cannot be given here, because no measurements with HERMES models have been performed so far in F4. The

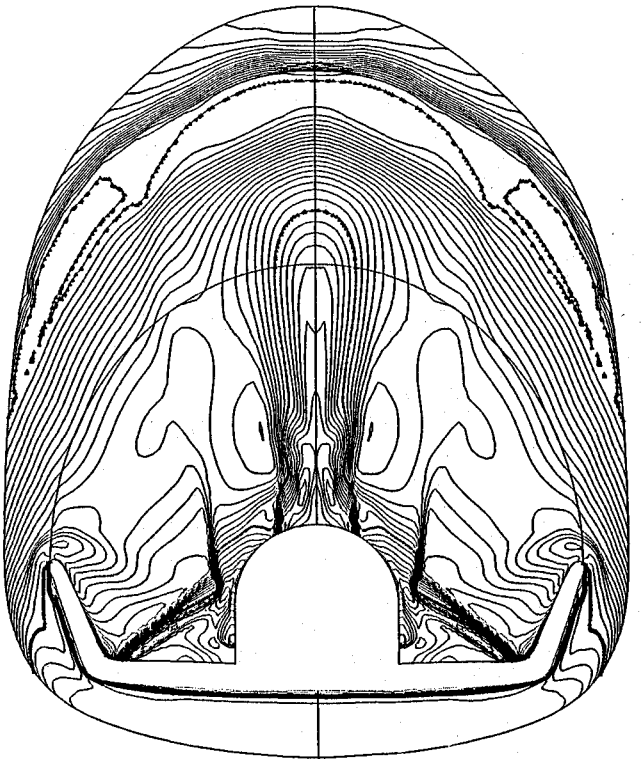

Fig. 3 HERMES 1.0, nonequilibrium Euler simulation. Mach number contours, Z = 14 m (fine). M_∞ = 20, α = 30 deg, p_∞ = 2.106 Pa, ρ_∞ = 3.738 × 10^{-5} kg/m³.

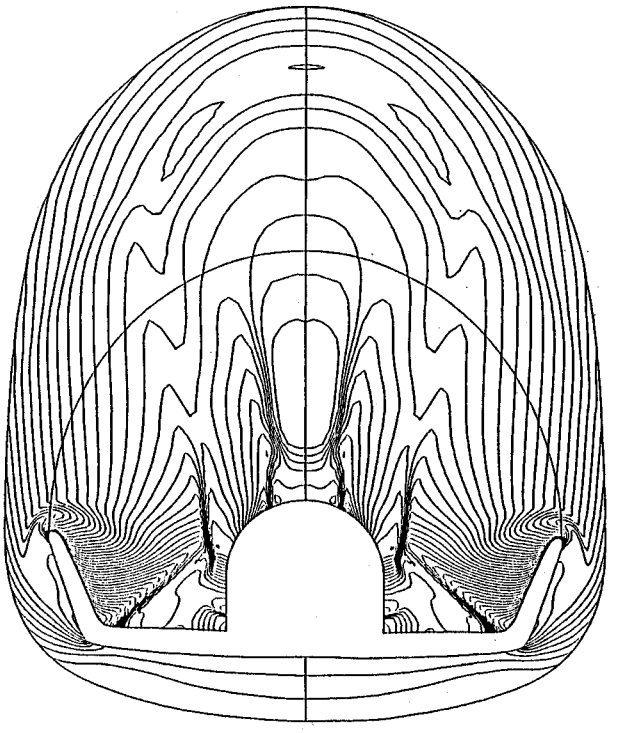

Fig. 4 HERMES 1.0, nonequilibrium Euler simulation. Isobars, log(p/p_∞), Z = 14 m (fine). M_∞ = 20, α = 30 deg, p_∞ = 2.106 Pa, ρ_∞ = 3.738 × 10^{-5} kg/m³.

same holds for the other high-enthalpy wind tunnel in Europe, the HEG of DLR in Göttingen, Germany. Comparing the global aerodynamic coefficients shown in Table 1, we see that for large Mach numbers the Mach number itself has almost no influence on the coefficients, whereas the angle of attack is very important. The variation from coarse grid to fine grid solution is small in the coefficients, justifying the use of the coarse mesh for global flow values. The pitching moment

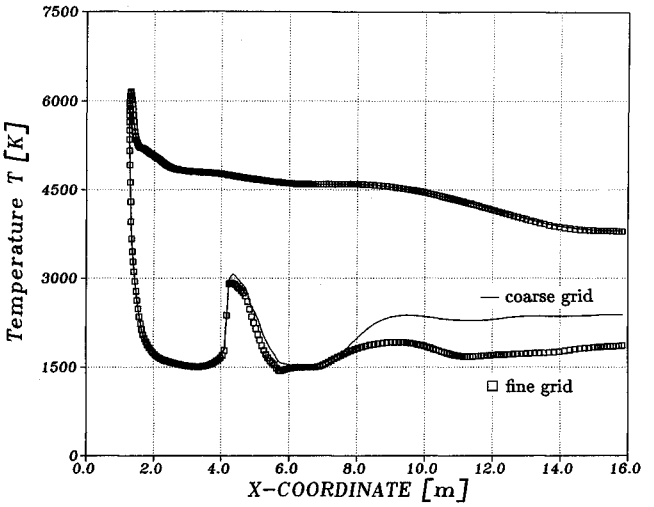

Fig. 5 HERMES 1.0, nonequilibrium Euler simulation. Surface temperature in symmetry plane (solid line: coarse, squares: fine). M_∞ = 20, α = 30 deg, p_∞ = 2.106 Pa, ρ_∞ = 3.738 × 10^{-5} kg/m³.

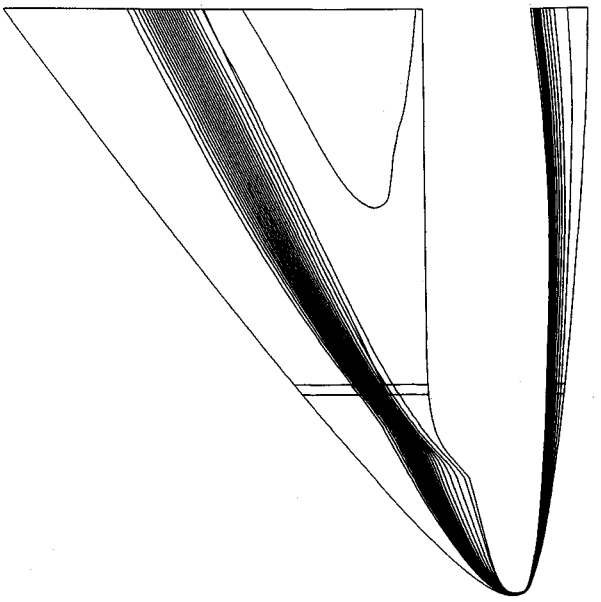

Fig. 6 HERMES 1.0, nonequilibrium Euler simulation. Atomic oxygen concentration y_0 in symmetry plane (fine). M_∞ = 20, α = 30 deg, ρ_∞ = 2.106 Pa, p_∞ = 3.738 × 10^{-5} kg/m³.

(p.m.) is a much more sensitive parameter than the lift and drag coefficient.

B. Generic Configurations

In the second part, we analyze viscous nonequilibrium flows over generic configurations. The transport model used in the computations is Blottner's model for the species viscosities, Eucken's correction for heat conductivities, and Wilke's mixing rule (BEW-model). For the hyperbola-flare flow, we employ additionally Yos' transport model. The first case considered here is the hypersonic flow over a double ellipse at M_∞ = 25, α = 30 deg, p_∞ = 2.52 Pa, T_∞ = 205 K, Re_∞ = 2.2 × 10^4 (H = 75 km), and T_{wall} = 1500 K. This case is identical to case VI.3 of the Antibes workshop.[32] Figure 7 shows Mach number contours for a grid consisting of 160 × 65 grid points (160 points in streamwise direction and 65 points in wall normal direction, exponential stretching). The canopy shocks is very different compared to an inviscid simulation. For viscous flow, the flow separates at the root of the canopy. Since the separation region smears out the kink in the body surface at the canopy root, the canopy shock of the inviscid

Table 1 Global coefficients, HERMES shape 1.0, nonequilibrium

Case no.	1	2	3	4	5	6
M_∞	12	12	12	12	20	25
Condition	F4	F4	F4	F4	H = 76 km	H = 76 km
p_∞, Pa	179.9	179.9	179.9	179.9	2.106	2.106
T_∞, K	249	249	249	249	196	196
α, deg	30	30	25	40	30	30
Lift	0.47874	0.47931	0.37302	0.66232	0.47198	0.46869
Drag	0.32980	0.33043	0.22184	0.62359	0.32559	0.32447
Pitching moment	0.00601	0.00572	0.00763	−0.00378	0.00743	0.00891
Grid	Fine	Coarse	Coarse	Coarse	Fine	Coarse

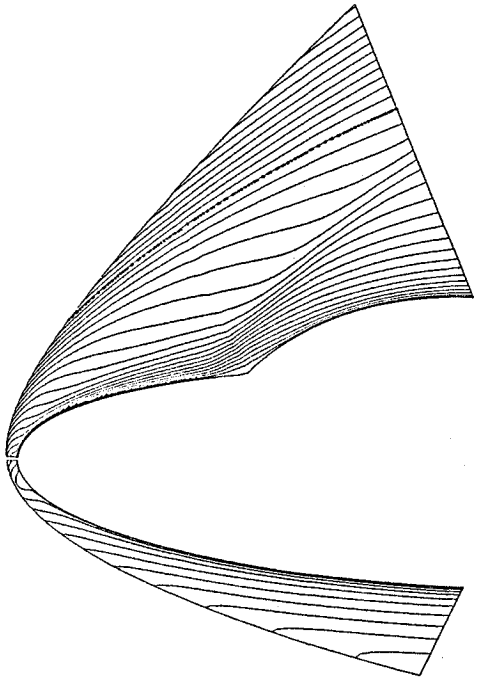

Fig. 7 Double-ellipse flow, nonequilibrium Navier-Stokes. Mach number contours, viscous flow. M_∞ = 25, α = 30 deg, p_∞ = 2.52 Pa, T_∞ = 205 K, Re_∞/m = 2.2 × 10^4, T_{wall} = 1500 K.

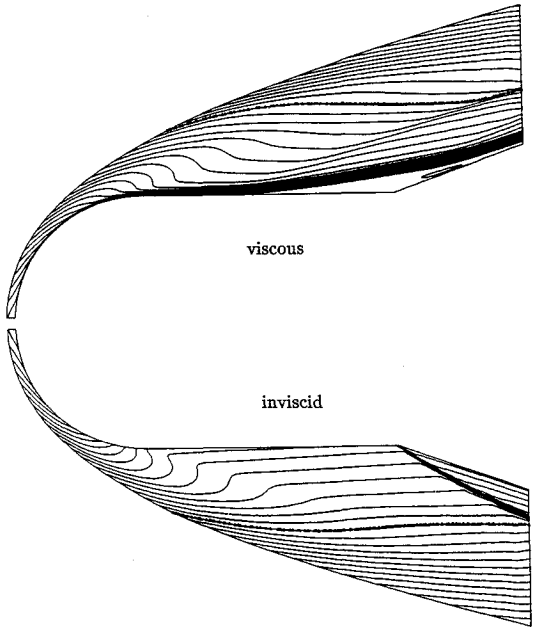

Fig. 8 Hemisphere-cylinder-flare flow, nonequilibrium Navier-Stokes. Mach number contours, viscous flow (upper half) and inviscid flow (lower half). M_∞ = 20, p_∞ = 22.5 Pa, T_∞ = 254 K, Re_∞/m = 1.1 × 10^5, T_{wall} = 1500 K.

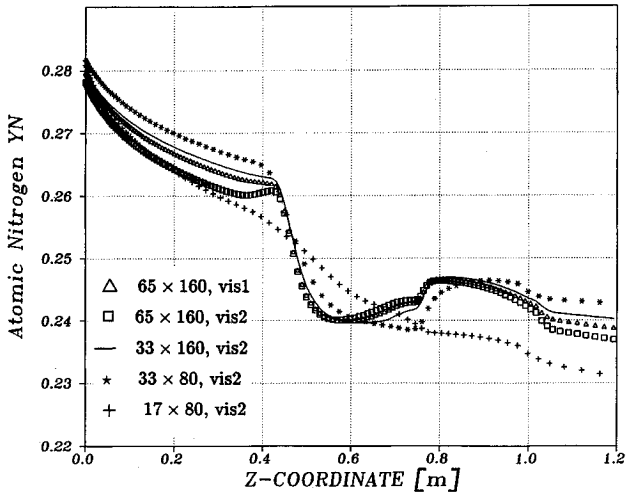

Fig. 9 Hyperbola-flare flow, nonequilibrium Navier-Stokes. Atomic nitrogen y_N concentration on surface. M_∞ = 25, p_∞ = 2.106 Pa, T_∞ = 196 K, Re_∞/m = 2 × 10^4, T_{wall} = 1500 K.

flow degenerates to a much weaker shock induced by the beginning of the separation region.

The next flow case is a hemisphere-cylinder-flare combination (axisymmetric) at M_∞ = 20, α = 0 deg, p_∞ = 22.5 Pa, T_∞ = 254 K, Re_∞/m = 1.1 × 10^5 (H = 60 km), and T_{wall} = 1500 K. The upper half of Fig. 8 presents Mach number contours for viscous flow with a mesh consisting of 80 × 65 grid points. The lower half displays Mach number contours for inviscid flow with a resolution of 80 × 33 grid points. As for the double ellipse flow, the inviscid flare shock degenerates to a weak separation shock generated at the beginning of the large separation region at the cylinder-flare intersection. Due to the very different boundary conditions in inviscid and viscous flow, mass concentrations on the body surface differ greatly in both cases ($y_{N,viscous} \approx 0.21$, $y_{N,inviscid} \approx 0.35$). In inviscid flow, the body temperature is high, leading to increased dissociation of molecular nitrogen at the body surface. For viscous flow, an isothermal wall is assumed with a (compared to inviscid flow) low wall temperature of T_{wall} = 1500 K.

The influence of both grid resolution and transport models is analyzed in the third flow case, the flow over a hyperbola-flare (two-dimensional). The flow conditions are M_∞ = 25, p_∞ = 2.106 Pa, T_∞ = 196 K, Re_∞/m = 2 × 10^4 (H = 76 km), and T_{wall} = 1500 K. Figure 9 shows mass concentrations of atomic nitrogen on the surface of the hyperbola-flare. The flare begins at Z = 0.75 m. Two fine grid results are shown computed with a mesh consisting of 160 × 65 points in streamwise and wall normal direction, respectively (exponential stretching). The squares denote the solution obtained with Yos' transport model, and the triangles denote the standard transport model (BEW) solution. The differences in both solutions in the hyperbola-part can be explained by the freestream Reynolds number. Due to the different models the freestream Reynolds numbers Re_∞/m are Re_∞/m = 2.09 × 10^4

for Yos' model and $Re_\infty/m = 1.73 \times 10^4$ for the BEW model. The freestream Reynolds number based on Sutherland's viscosity law is $Re_\infty/m = 2.035 \times 10^4$. The other curves which correspond to the BEW model show the influence of mesh resolution. The solid line denotes a solution obtained with a 160×33 mesh, the stars correspond to a resolution of 80×33 points, and the plus-signs correspond to a 80×17 mesh, all of them computed employing the BEW model. In the rear part after separation, the influence of mesh resolution on the solution is larger than the influence of different transport models. This is inversed for the front part (up to separation). The coarsest grid (80×17 points) cannot detect the separation accurately due to an insufficient resolution of the viscous layer. A more detailed description of the results is given in Menne et al.[29]

V. Conclusions

The solution method described in this article was developed for the numerical simulation of nonequilibrium real gas flows about the complete HERMES configuration. The inviscid results to the flow about HERMES 1.0 show the applicability of the presented algorithm to three-dimensional nonequilibrium hypersonic flows over realistic configurations. The coarse grid solution is usually sufficient to describe global flow features as well as aerodynamic loads. The analysis of local flow phenomena requires refined meshes. The extension of the nonequilibrium Euler algorithm to viscous flows is demonstrated by an application of the Navier-Stokes solver to several generic configurations. The quasiconservative formulation with matrix-splitting turns out to allow an accurate description of nonequilibrium flows in both inviscid and viscosity dominated regions. The combination with Runge-Kutta time stepping, high-order upwinding, and shock-fitting leads to an efficient, accurate, and reliable solution method that is used routinely to analyze both complete flowfields and local flow phenomena for selected trajectory points. The flow examples presented in this article constitute only a sample of the flow cases investigated with the current code. In the near future, the code will be extended to thermal nonequilibrium, wall catalycity models, and advanced transport models.

References

[1]Gnoffo, P. A., and McCandless, R. S., "Three-Dimensional AOTV Flowfields in Chemical Nonequilibrium," AIAA Paper 86-0230, Jan. 1986.

[2]Candler, G. V., and MacCormack, R. W., "The Computation of Hypersonic Ionized Flows in Chemical and Thermal Nonequilibrium," AIAA Paper 88-0511, Jan. 1988.

[3]Palaniswamy, S., Chakravarthy, S. R., and Ota, D. K., "Finite-Rate Chemistry for USA—Series Code: Formulation and Applications," AIAA Paper 89-0200, Jan. 1989.

[4]Shuen, J. S., "Upwind Differencing and LU Factorization for Chemical Non-Equilibrium Navier-Stokes Equations," *Journal of Computational Physics*, Vol. 99, No. 2, 1992, pp. 233–250.

[5]Imlay, S. T., Roberts, D. W., Soetrisno, M., and Eberhardt, S., "Nonequilibrium Thermo-Chemical Calculations Using a Diagonal Implicit Scheme," AIAA Paper 91-0468, Jan. 1991.

[6]Netterfield, M. P., "Validation of a Navier-Stokes Code for Thermochemical Non-Equilibrium Flows," AIAA Paper 92-2878, July 1992.

[7]Weiland, C., "A Split-Matrix Method for the Integration of the Quasi-Conservative Euler Equations," *Notes on Numerical Fluid Mechanics*, Vol. 13, Vieweg, Braunschweig, 1986, pp. 383–390.

[8]Weiland, C., and Pfitzner, M., "3-D and 2-D Solutions of the Quasi-Conservative Euler Equations," *Lecture Notes in Physics*, Vol. 264, Springer-Verlag, Berlin, 1986, pp. 654–659.

[9]Pfitzner, M., and Weiland, C., "3-D Euler Solutions for Hypersonic Mach Numbers," AGARD-CP 428, Paper 22, Bristol, England, Loughton, UK, 1987.

[10]Pfitzner, M., "Runge-Kutta Split-Matrix Method for the Simulation of Real Gas Hypersonic Flows," *Notes on Numerical Fluid Mechanics*, Vol. 24, Vieweg, Braunschweig, 1988, pp. 489–498.

[11]Pfitzner, M., "A 3-D Non-Equilibrium Shock-Fitting Algorithm Using Effective Rankine-Hugoniot Relations," AIAA Paper 91-1467, June 1991.

[12]Pandolfi, M., "Upwind Formulations for the Euler Equations," *Lecture Series*, 1987-04, Von Karman Inst., Brussels, Belgium, 1987.

[13]Kee, R. J., Miller, J. A., and Jefferson, T. H., "CHEMKIN: A General Purpose, Problem-Independent, Transportable, Fortran Chemical Kinetics Code Package," Sandia Labs., Rept. SAND80-8003, Albuquerque, NM, 1980.

[14]Pfitzner, M., "Simulations of Inviscid Equilibrium and Nonequilibrium Hypersonic Flows," *Lecture Notes in Physics*, Vol. 371, Springer-Verlag, Berlin, 1986, pp. 432–436.

[15]Park, C., "On the Convergence of Computation of Chemically Reacting Flows," AIAA Paper 85-0247, Jan. 1985.

[16]Park, C., "Problems of Rate Chemistry in the Flight Regions of Aeroassisted Orbital Transfer Vehicles," Vol. 96, Progress in Astronautics and Aeronautics, AIAA, New York, 1985, pp. 511–537.

[17]Vincenti, W. G., and Kruger, C. H., *Introduction to Physical Gas Dynamics*, Wiley, New York, 1966, Chap. 7.

[18]Bird, R. B., Stewart, W. E., and Lightfood, E. N., *Transport Phenomena*, Wiley, New York, 1960, Chap. 3.

[19]Blottner, F. G., Johnson, M., and Ellis, M., "Chemically Reacting Viscous Flow Program for Multi-Component Gas Mixtures," Sandia Labs., Rept. SC-RR-70-754, Albuquerque, NM, 1971.

[20]Oertel, H., *Stoßrohre*, Springer-Verlag, Wien, 1966, Chap. B.5.

[21]Wilke, C. R., "A Viscosity Equation for Gas Mixtures," *Journal of Chemical Physics*, Vol. 18, No. 4, 1950, pp. 517–522.

[22]Candler, G., "The Computation of Weakly Ionized Hypersonic Flows in Thermo-Chemical Nonequilibrium," Ph.D. Dissertation, Stanford Univ., Stanford, CA, 1988, pp. 21, 22.

[23]Desideri, J. A., "Technical Document," Workshop on Hypersonic Flows for Reentry Problems, Part II, Antibes, France, INRIA, Sophia-Antipolis, Jan. 1991.

[24]Yos, J. M., "Transport Properties of Nitrogen, Hydrogen, Oxygen, and Air to 30,000° K," AVCO Corp., RAD-TM-63-7, March, 1963.

[25]Gnoffo, P. M., Gupta, R. N., and Shinn, J. L., "Conservation Equations and Physical Models for Hypersonic Air Flows in Thermal and Chemical Nonequilibrium," NASA TP-2867, 1989.

[26]Poeppe, C., "Explicit Euler Solver for Chemically Reacting Flows," HERMES Research Rept. ESA/CNES, Heidelberg, H-DS-1-1059-AMD, Feb. 1989.

[27]Menne, S., "Efficient Solution of Three-Dimensional Viscous Hypersonic Flows," *Aerothermodynamics for Space Vehicles*, ESA SP-318, ESTEC, Noordwijk, The Netherlands, 1991, pp. 267–272.

[28]Menne, S., and Weiland, C., "Calculation of Three-Dimensional Viscous and Inviscid Hypersonic Flows Using Split-Matrix Marching Methods," AIAA Paper 90-3070, Aug. 1990.

[29]Menne, S., Weiland, C., and Pfitzner, M., "Computation of 3-D Hypersonic Flows in Chemical Non-Equilibrium Including Transport Phenomena," AIAA Paper 92-2876, July 1992.

[30]Whitfield, D. L., and Janus, J. M., "Three-Dimensional Unsteady Euler Equations Solution Using Flux Vector Splitting," AIAA Paper 84-1552, June 1984.

[31]Hartmann, G., and Weiland, C., "Strömungsfeldberechnungen um den HERMES Raumgleiter während der Wiedereintrittsphase," *DGLR Jahrbuch 1991*, Paper 91-223, 1991, pp. 255–264.

[32]Workshop on Hypersonic Flows for Reentry Problems, Part II, INRIA, GAMNI-SMAI, Antibes, France, April 1991.